

## Research Article

# Mechanical Characterization of Reduced Graphene Oxide Using AFM

**Alem Teklu , Canyon Barry, Matthew Palumbo, Collin Weiwadel, Narayanan Kuthirummal, and Jason Flagg**

*Department of Physics and Astronomy, College of Charleston, Charleston, SC, USA*

Correspondence should be addressed to Alem Teklu; [teklua@cofc.edu](mailto:teklua@cofc.edu)

Received 20 August 2018; Revised 21 November 2018; Accepted 6 December 2018; Published 2 January 2019

Guest Editor: Hong Fang

Copyright © 2019 Alem Teklu et al. This is an open access article distributed under the Creative Commons Attribution License, which permits unrestricted use, distribution, and reproduction in any medium, provided the original work is properly cited.

Nanoindentation coupled with Atomic Force Microscopy was used to study stiffness, hardness, and the reduced Young's modulus of reduced graphene oxide. Oxygen reduction on the graphene oxide sample was performed via LightScribe DVD burner reduction, a cost-effective approach with potential for large scale graphene production. The reduction of oxygen in the graphene oxide sample was estimated to about 10 percent using FTIR spectroscopic analysis. Images of the various samples were captured after each reduction cycle using Atomic Force Microscopy. Elastic and spectroscopic analyses were performed on the samples after each oxygen reduction cycle in the LightScribe, thus allowing for a comparison of stiffness, hardness, and the reduced Young's modulus based on the number of reduction cycles. The highest values obtained were after the fifth and final reduction cycle, yielding a stiffness of 22.4 N/m, a hardness of 0.55 GPa, and a reduced Young's modulus of 1.62 GPa as compared to a stiffness of 22.8 N/m, a hardness of 0.58 GPa, and a reduced Young's modulus of 1.84 GPa for a commercially purchased graphene film made by CVD. This data was then compared to the expected values of pristine single layer graphene. Furthermore, two RC circuits were built, one using a parallel plate capacitors made of light scribed graphene on a kapton substrate (LSGC) and a second one using a CVD deposited graphene on aluminum (CVDGC). Their RC time constants and surface charge densities were compared.

## 1. Introduction

The unique one-atom-thick two-dimensional structure of carbon nanomaterial graphene must continually be examined as it exhibits many desired mechanical, electrical, thermal, and optical properties [1]. These properties influence and affect surface area, conductivity, the quantum hall effect, electron scattering, band structure, and the Klein paradox [2].

Even though graphene is well studied, its large scale commercial production still proves challenging and expensive [3, 4]. Thus, there is a high likelihood that many scientists will attempt to develop new and cost-effective graphene fabricating techniques [5, 6]. As such, this work focuses on the importance of examining the properties of homemade reduced graphene oxide that proves to be significant for interpreting future scientific investigations. We used LightScribe DVD burner, a cost-effective approach with potential for large scale graphene production. Yet, not much work has been done on the elastic or mechanical

properties of such large size two-dimensional homemade films of reduced graphene oxide samples. Therefore, in this work, we used nanoindentation coupled with Atomic Force Microscopy (AFM) in order to obtain better understanding of the structure and the mechanical properties of both homemade reduced graphene oxide and commercially purchased graphene (made by chemical-vapor deposition). The main investigation surrounding homemade reduced graphene oxide revolves around measuring the difference in stiffness, hardness, and the reduced Young's modulus of samples based on the number of trips through a LightScribe DVD burner [7]. Images of each sample were captured after its oxygen reduction cycle in the LightScribe. These results were then compared to the experimentally determined values for the reduced Young's modulus of a commercially purchased sample, as well as the expected theoretical value for pristine graphene. Two properties of graphene that are important for its use in electrical applications (such as supercapacitors) is that it consists of a honeycomb arrangement of carbon atoms

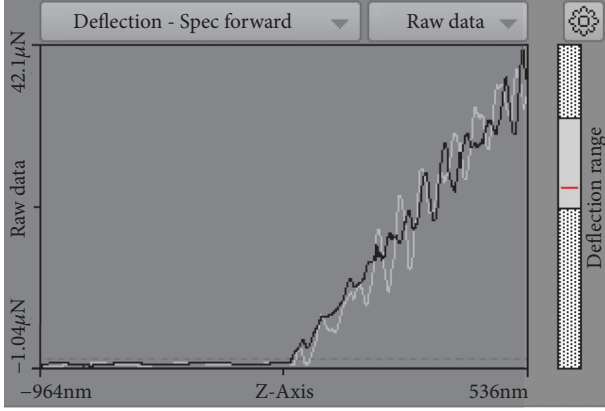


FIGURE 1: Force-distance curve for graphene oxide. The white line depicts the loading stage, while the black line represents the unloading stage.

that is one-atom thick allowing a high specific surface area and that it has a high electron mobility. Thus, two parallel plate capacitors were built using laser-scribed graphene on a kapton substrate as the electrodes for one (LSGC), and chemical-vapor deposited graphene on an aluminum foil substrate as the electrodes for the other (CVDGC).

## 2. Theory

Nanoindentation serves as one of the most common means of testing mechanical properties of materials. Once calibrated, the Atomic Force Microscope (AFM) measures the intensity of interactions between a probe and the sample during the loading stage (indentation) and the unloading stage (while the probe is retracted). The small area of the probe tip, which comes in various shapes, allows for a high sensitivity to minuscule forces. The probe tips are placed on soft springs (cantilevers), which are often made of silicon, allowing for detection of forces in the range of a few nN [8]. These subtle interactions are recorded on a force-distance curve as shown in Figure 1. From this curve, numerous mechanical properties of thin-films and characteristics can be derived.

**2.1. Imaging.** The Nanosurf Flex Atomic Force Microscope and AFMs in general are widely used to create both two and three-dimensional surface images [10]. These images are accurate on a nanometer scale and can be taken using both contact and noncontact probes.

Along with high resolution imaging, the Nanosurf can also be used for various spectroscopic investigations, in this instance, nanoindentation. The calibration of the AFM allows the indentation measurements to be taken in nano-Newtons based on the cantilever spring constant instead of voltage based on the scan head calibration. This allows for derivations of stiffness, hardness, and the reduced Young's modulus based on the force-distance curve.

**2.2. Force Spectroscopy and Nanoindentation.** In force spectroscopy mode the AFM probe is used as an indenter.

Depending on the spring constant and strength of the indenting probe, vertical forces are applied ranging from  $\mu\text{N}$  to tens of pN. When indenting a surface on a nanometric scale, many atomic forces interact with the attraction and separation of the probe leading to distinct stages of the cantilever deflection and force-distance curve. As the cantilever approaches the sample with just nanometers of separation, atomic van der Waals forces attract the probe to jump-to-contact resulting in a negative vertical force measurement. After physical contact, continued vertical force is applied to the sample causing elastic and plastic deformation; this is the loading stage. Subsequently, once the max force  $P_{max}$  is reached the cantilever is retracted. The release of pressure is measured and visualized in the unloading stage. In the last phase of cantilever retraction, adhesion forces between the probe and sample cause a jump-off-contact point where, again, negative vertical forces are measured. Though these adhesive and attractive forces give insight into the electrostatic properties of the sample, nanomechanical and structural characteristics are extracted from the contour of the unloading stage in the force-distance curve. Figure 2 shows an idea force-distance curve with respective loading and unloading stages. The nanometric contact nature between the AFM probe and sample makes the accurate measurement of necessary parameters, such as the area of probe contact ( $A_c$ ), challenging. Thus, many methods have been introduced to accurately model the tip-sample interaction while enabling a derivation of relevant structural characteristics. Our analysis used AtomicJ [11] for determining the stiffness and reduced Young's modulus and the widely accepted method proposed by Oliver and Pharr for determining the hardness. This relationship is given in Equation (4).

Using the Oliver and Pharr model, three main characteristics must be measured from the force-distance curve: the maximum applied load,  $P_{max}$  (N), the displacement at  $P_{max}$ ,  $h_{max}(m)$ , and the contact stiffness,  $S$ . Once these quantities are measured, the projected cross sectional area of the indenter,  $A(h_c)(m^2)$ , is calculated using  $h_c$ , the residual contact depth, and a conical approximation of the probes dimensions using the manufacturer's specifications. Figure 3 shows the probe manufacturers tetrahedral tip dimensions used for calculating the conical cross section.

Figure 4 shows an ideal indentation to visualize the contact depth,  $h_c$  [see (1)], and subsequent projected cross-sectional area equation [see (2)]. The contact depth is written as

$$h_c = h_{max} - \epsilon \left( \frac{P_{max}}{S} \right) \quad (1)$$

where  $\epsilon = 0.75$ , constant for conical tip indenter. Similarly, the projected area is given by

$$A(h_c) = (\pi) [\tan(18^\circ)(h_c)]^2 \quad (2)$$

As seen in Figure 2, contact stiffness,  $S$ , is calculated to be the slope of the unloading curve. Because the upper portion of the unloading curve corresponds to the linear stage of the probe retraction before tapering off, the most

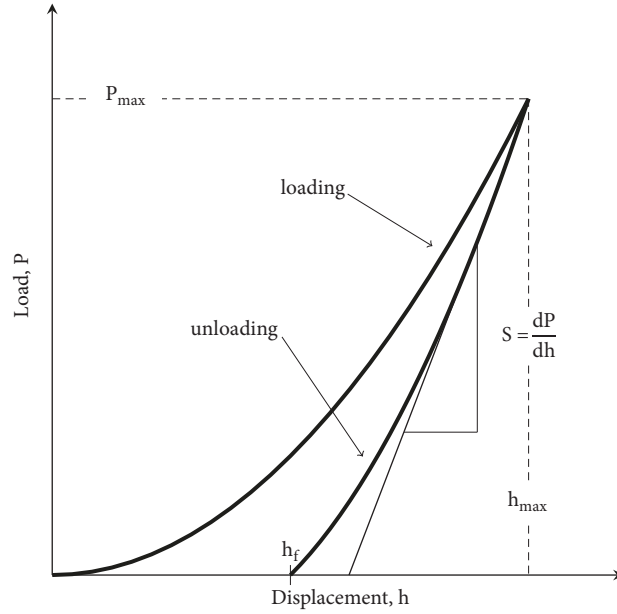


FIGURE 2: Force-distance curve for graphene oxide. The white line depicts the loading stage, while the black line represents the unloading stage.

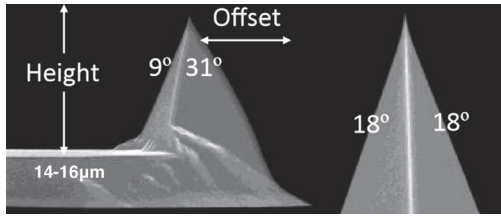


FIGURE 3: This figure, provided by AppNano, shows the dimensions of the tetrahedral tip.

accurate stiffness measurements are calculated from this initial gradient. Mathematically,

$$S = \left( \frac{\partial P}{\partial h} \right). \quad (3)$$

Once contact area is determined, the hardness,  $H$ , defined as the mean pressure a substance can support across that area, is calculated using the equation

$$H = \frac{P_{max}}{A(h_c)} \quad (4)$$

where  $P_{max}$  is the max load (N) and  $A$  is the contact area during indentation ( $m^2$ ) [12].

Young's modulus is a measure of elasticity or the stress and strain ratio of a substance. Because of elastic nature of the unloading curve, the reduced or effective Young's modulus was calculated [13]. Using the stiffness from Equation (3) and the contact area from Equation (2), the reduced elastic

modulus takes elastic deformations in both the probe and sample into account and is given by

$$E_r = \frac{S\sqrt{\pi}}{2\sqrt{A}(h_c)}, \quad (5)$$

where  $E_r$  is the reduced Young's modulus (Pa).

### 3. Methodology

**3.1. Production of Graphene.** For large scale top-down synthesis of graphene, it begins with a block of graphite. Because graphite is simply billions of graphene sheets stacked together, the introduction of strong acids oxidize the substance into graphene oxide. Oxidation weakens the chemical bonding thus creating a greater interlayer spacing between them. A final thermal shock of the graphene oxide at high temperature enables an opening of the structure creating graphene platelets with a thickness of 1-2 nm. Homemade graphene specimens were produced with a similar top-down approach using a commercially purchased 60 ml aqueous solution of graphene oxide (GO). Comprised of 5 g/L of graphene oxide, this highly concentrated solvent enables samples to be prepared of varying sizes and shapes. The graphene oxide used in the solution was approximately 79% carbon and 20% oxygen [14]. Ensuring that the graphene oxide mixture was uniformly and consistently spread over the entire sample area, the solution was placed in an ultrasonic cleaner. The uniformly mixed solvent was siphoned on to a polytetrafluoroethylene (PTFE) substrate and was dried using two methods: standard air-drying, as well as curing in a vacuum oven for 24 hours at 100°C and 70 mmHg below standard atmospheric pressure. (Air-dried samples developed a nonuniform profile with enclosed air bubbles

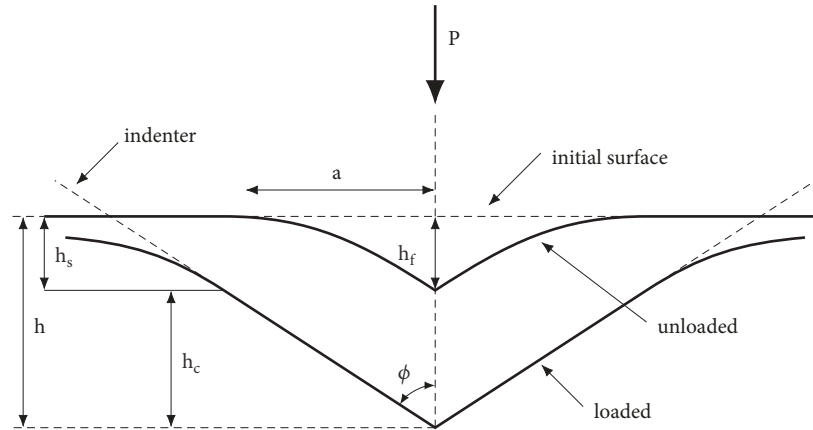


FIGURE 4: Ideal indentation depicting  $h_c$  and the initial linear portion of the unloading stage where stiffness is calculated.

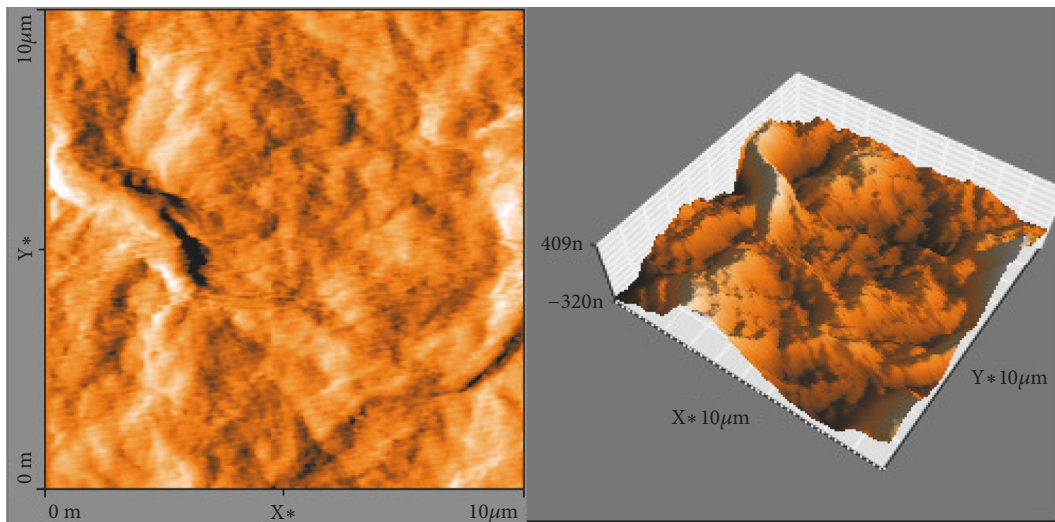


FIGURE 5: AFM image and three-dimensional topography of **air-dried graphene oxide solution** taken using the DD-ACTA probe. The sample shows a region of elevated height with crater structure seen in the upper left hand corner of the three-dimensional topography scan.

leading to vast deviations in topography and indentation characteristics.) Once cured the samples were adhered to a standard, writable compact disk in order to perform a thermal shock via the high intensity laser in a LightScribe drive resulting in oxygen reduction [15]. Producing graphene on PTFE substrates do not alter their composition and enable samples be easily transferred to the CD for oxygen reduction cycles or to glass slides for examination. AFM images of air-dried and vacuum-dried graphene oxide samples are shown in Figures 5 and 6, respectively.

Conversely, the commercially purchased graphene used for comparison was fabricated through chemical-vapor deposition (CVD), a bottom-up procedure. Though this process can grow graphene on various substrates such as copper or nickel, our samples were coated a sheet of aluminum foil. The graphene coating had an average thickness of 3.5 nm, and the lateral size of the individual graphene flakes were between 5-10  $\mu\text{m}$  [9]. These flakes coated the surface to form a conductive layer. SEM images taken by the manufacturer

and AFM images showing similar flake patterns taken by our group are compared in Figures 7 and 8, respectively.

**3.2. AFM Calibration.** The first step in setting up the AFM for imaging and spectroscopic analysis involved mounting a probe. For this experiment, noncontact AppNano ACLA [16], contact AppNano SHOCON probes [17], and AppNano Diamond Doped ACTA probes (DD-ACTA) [18] were used. Mounting the probe on the cantilever holder was usually done with forceps, while vacuum tweezers were utilized when removing the probe for storage. Proper mounting proved crucial for ideal laser alignment and accurate measurements.

Once a probe had been mounted, the laser must be aligned on the probe tip. Alignment was achieved by adjusting the laser's position through a viewing port on the AFM. Course X/Y direction adjustments were performed first, while examining the laser working point meter provided in the Nanosurf EasyScan 2 software.

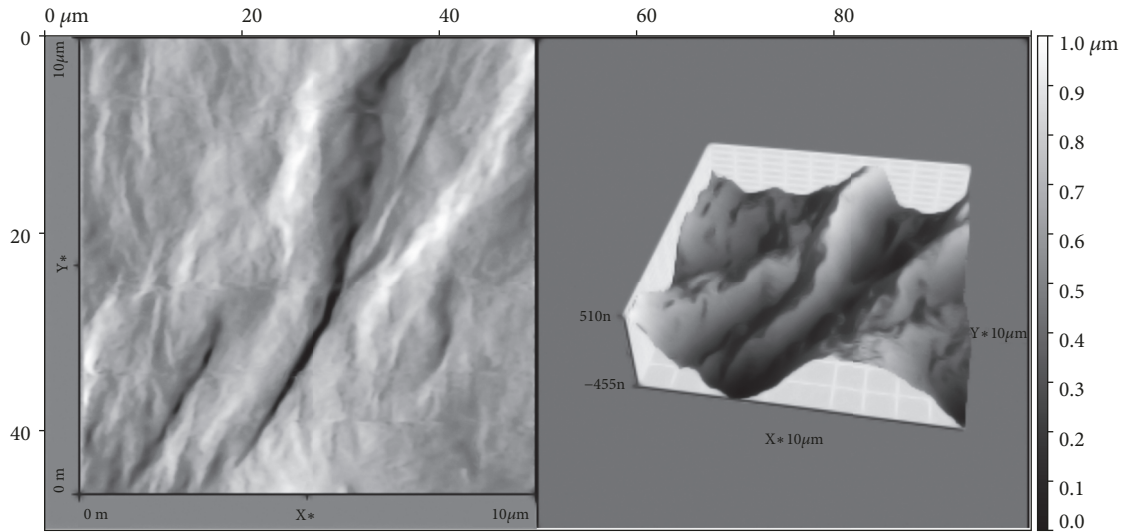


FIGURE 6: AFM image and three-dimensional topography of **vacuum oven-dried graphene oxide solution** taken using the DD-ACTA probe. A crevasse region runs through the center of the sample, with elevated regions on either side.

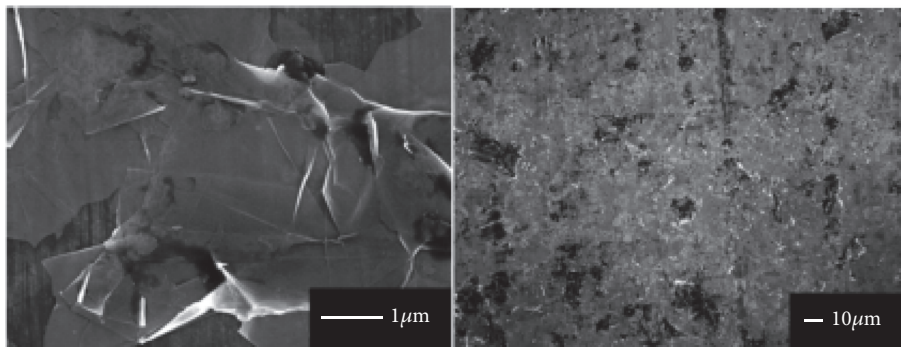


FIGURE 7: SEM images taken by the supplier of the graphene coated aluminum [9]. Although the  $1\ \mu\text{m}$  resolution of one the suppliers images is greater than what the AFM can accurately image, the flake-like structures clearly resemble each other.

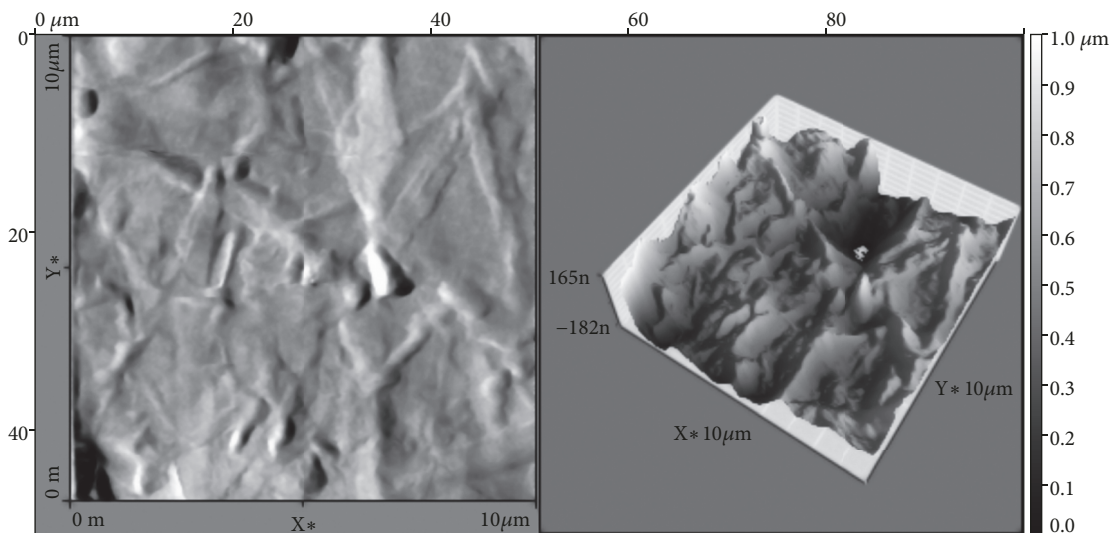


FIGURE 8: AFM image and three-dimensional topography of **commercially purchased graphene coated aluminum**. Again, graphene flakes are easily seen in the two-dimensional AFM image on the left. These images were taken using the DD-ACTA probe.

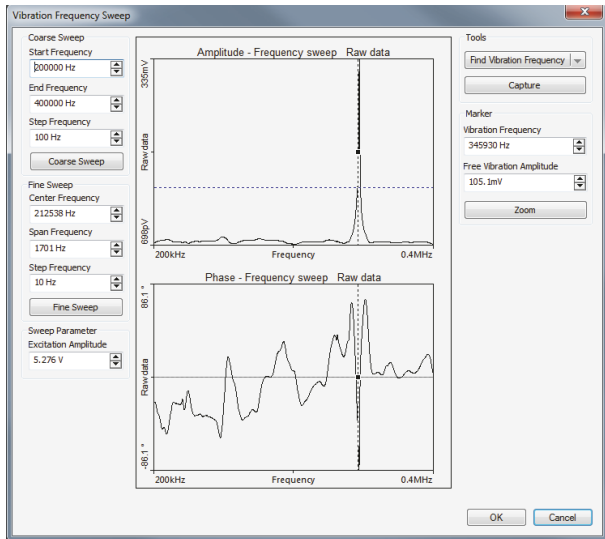


FIGURE 9: This figure shows the Vibration Frequency Search Dialogue for the Nanosurf EasyScan 2 software using the DD-ACTA probe. The frequency range was set between 200 and 400 kHz, with the peak frequency occurring at 346 kHz.

A coarse frequency sweep was then performed, again utilizing the Nanosurf EasyScan 2 software. Depending on the probe used, the frequency range was set (see the Start Frequency and End Frequency entries in the upper left corner of Figure 9) and a course sweep was performed to determine the free resonant frequency. This graph was then exported as a .plt file to the program *springconstant.exe*, which determines the experimental spring constant of the probe. In our experiment, the spring constant of the SHOCON contact probe was 0.148 N/m and that of the DD-ACTA probe was 40 N/m. Finding the experimental spring constant proved significant, as the manufacturer's specifications displayed a wide range with significant error. This value also allowed for force-distance curve measurements to be converted to Newtons rather than left as voltage based on the scan head calibration.

One final step before data could be collected involved determining the deflection sensitivity of the instrument. For this test, a hard sapphire crystal was used as a calibration tool. An indentation was performed and a force-distance graph was obtained. The slope of the unloading portion of the graph was determined using the measure length feature of the Nanosurf EasyScan 2 software. This value was given in units of Volts per meter. Based on these calibration measurements, the deflection sensitivity for the DD-ACTA probe was calculated to be 984 nm.

**3.3. Images and Topography.** Once calibrated, the AFM was used to image the samples as well as measure the stiffness, hardness, and reduced Young's modulus. Numerous images, as well as a total of thirty data points were taken for each sample after each trip through the LightScribe. At each data point, an indentation occurred, where the force of the loading and unloading phases were recorded on a

force-distance curve. This curve was then used to derive the above values as outlined in the Theory section. Ten different data points were selected on a  $10\ \mu\text{m}$  by  $10\ \mu\text{m}$  area on the sample before physically moving the sample to test another area. This process was repeated two additional times to obtain the thirty points, which were then averaged to obtain the final values. These values were recorded for the homemade samples after each trip through a LightScribe oxygen reduction cycle, as well as for the commercially purchased graphene. It is important to note, that the same sample could not be used throughout experimentation. After performing nanoindentation at thirty different points on the sample, the structure and hence the surface mechanical properties of the sample could be compromised. Because all the samples were made in the same way under the same circumstances, it was practical to use a different sample after each nanoindentation measurements without any loose of generality. As a result, a total of 7 samples were produced and tested: untreated air-dried graphene oxide, untreated vacuum oven-dried graphene oxide, 1 reduction cycle graphene oxide, 2 reduction cycle graphene oxide, 3 reduction cycle graphene oxide, 4 reduction cycle graphene oxide, and 5 reduction cycle graphene oxide.

**3.4. RC Measurement.** The laser-scribed graphene capacitor (LSGC) was built by first cutting kapton into two  $2.5\ \text{cm} \times 2.5\ \text{cm}$  squares with  $1\ \text{cm} \times 1\ \text{cm}$  leads attached to them. These squares were then adhered to the top of a LightScribe enabled DVD disc. A graphene oxide dispersion of  $5\ \text{g/L}$  of water was then drop casted onto the adhered kapton substrates. The sample was then allowed to dry at ambient conditions. Once dried the disc was then inserted into the LightScribe DVD burner upside down allowing the laser to etch the surface. This process has then reduced the oxygen content in the graphene oxide, leaving us two graphene electrodes for our capacitor. After removing the electrodes from the disc they were sandwiched together with a Mylar dielectric in between them, which has a dielectric constant of 3.1 and a thickness of 25.4 microns. The graphene samples were also measured for their thickness using the Nanosurf EasyScan2 AFM. The LSG was shown to have a thickness of around 3-3.5 microns. As with the CVD made graphene capacitor, the aluminum substrate with the CVD graphene deposited onto it was cut into two  $2.5\ \text{cm} \times 2.5\ \text{cm}$  squares with  $1\ \text{cm} \times 1\ \text{cm}$  squares leads attached to them. The same Mylar substrate was used as a separator for this capacitor and constructed identically, but with aluminum instead of kapton.

## 4. Results and Discussion

**4.1. AFM Images.** Images were taken using the ACLA non-contact probe, the SHOCON contact probe, and the Diamond Doped ACTA probe. Image size varied between  $10\ \mu\text{m}$  to  $40\ \mu\text{m} \times 40\ \mu\text{m}$ , with the time per line set between 0.6-0.8 seconds (1024 lines per image). Images of graphene oxide were taken before attempted reduction to graphene occurred, as well as after each trip through a LightScribe reduction cycle. Figure 10 shows an image of a graphene oxide

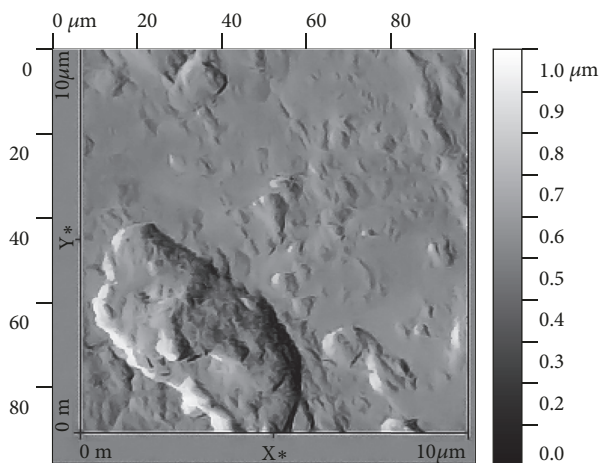


FIGURE 10: Image of a graphene oxide flake via SHOCON contact probe, taken prior to mixing into a solution to be reduced by the LightScribe. This is the only image taken of a graphene oxide flake that did not come purchased in premade solution.

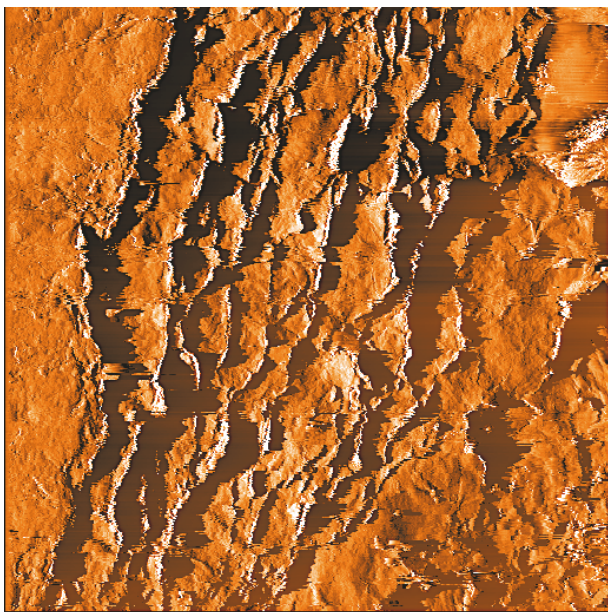


FIGURE 11: This image, taken with the SHOCON contact probe, clearly depicts the stratified nature of the graphene oxide sample. The scale length is  $40\ \mu\text{m}$  by  $40\ \mu\text{m}$  and the sample underwent 4 reduction cycles with the LightScribe.

flake before mixing it into a solution to be reduced by a LightScribe.

Images were then taken and were paired with their corresponding three-dimensional topography scan after each consecutive LightScribe reduction cycles. Representative images after the fourth and fifth oxygen reduction cycles are shown in Figures 11 and 12, respectively. Using this scan to perform three-dimensional analysis, it was possible to approximate both the number of layers of stacked graphene in the sample as well as an approximate height of the sample. Figure 11 represents AFM image of the graphene oxide sample after the

fourth reduction cycle with the LightScribe. Measurements of the various depths of the topography and edge positioning of the sample allowed for an approximation of the number of layers of stacked graphene to 5 layers. Figure 12 shows a two and three-dimensional images of AFM images after the fifth LightScribe reduction cycles of graphene oxide sample. Similar measurements of the various depths of the three-dimensional topography and edge positioning of the sample allowed for an approximation of the number of stacked graphene layers to 4-5 layers. As can be seen from these images, our group was able to produce high quality graphene oxide films with a simple cost-effective technique such as a LightScribe.

**4.2. SEM Images.** Towards the end of experiment, a scanning electron microscope (SEM) became available to image a 5 LightScribe reduction cycle sample. Figure 13 depicts flakes of graphene and stratified layers of the sample. The SEM was used to examine the sample from a larger scale. The image scales shown in the figure range from  $100\text{--}500\ \mu\text{m}$ . Attempts were made to take images on the same scale as the AFM ( $10\text{--}40\ \mu\text{m}$ ) but the resolution of the table-top SEM was not clear enough.

**4.3. Fourier Transform Infrared (FT-IR) Spectroscopy.** Fourier transform infrared (FTIR) photoacoustic spectra in the  $400\text{--}4000\ \text{cm}^{-1}$  were acquired by coadding 256 scans at a resolution of  $8\ \text{cm}^{-1}$  using a Varian 7000 FTIR spectrometer equipped with a MTS300 photoacoustic module from MTEC Photoacoustics, Inc. USA. Rapid scan was used to obtain the spectra of graphene samples in the solid state. The final spectra were light intensity normalized using photoacoustic signals from a carbon black pellet under the same experimental conditions. A typical spectrum of untreated graphene oxide sample and after it has undergone one to five oxygen reductions cycles via LightScribe is shown in Figure 14. Detailed analysis of the spectra revealed that there is a decrease in intensity of those bands involving oxygen in the  $1000\text{--}1800\ \text{cm}^{-1}$  (C-O stretching, C=O stretching, C-OH stretching, etc.) and  $3500\ \text{cm}^{-1}$  (O-H stretching) regions upon reducing the graphene oxide samples [19]. The largest oxygen reduction has been observed after the second reduction cycle. There were not significant changes after the third reduction cycle because the LightScribe reached its maximum reduction capabilities after this cycle. This result is consistent with the mechanical properties changes observed in nanoindentation measurements as shown in Figures 16–18.

**4.4. RC Analysis.** Each capacitor was connected in series with a resistor with an input  $60\ \text{kHz}$  AC square wave at  $10\ \text{V}$  peak to peak. The output waveform was analyzed using the cursor function of an oscilloscope to find the RC time constants. This process was repeated for ten different resistors for each capacitor. The maintained voltage, the RC time constant, the capacitance, and the average surface charge density where all

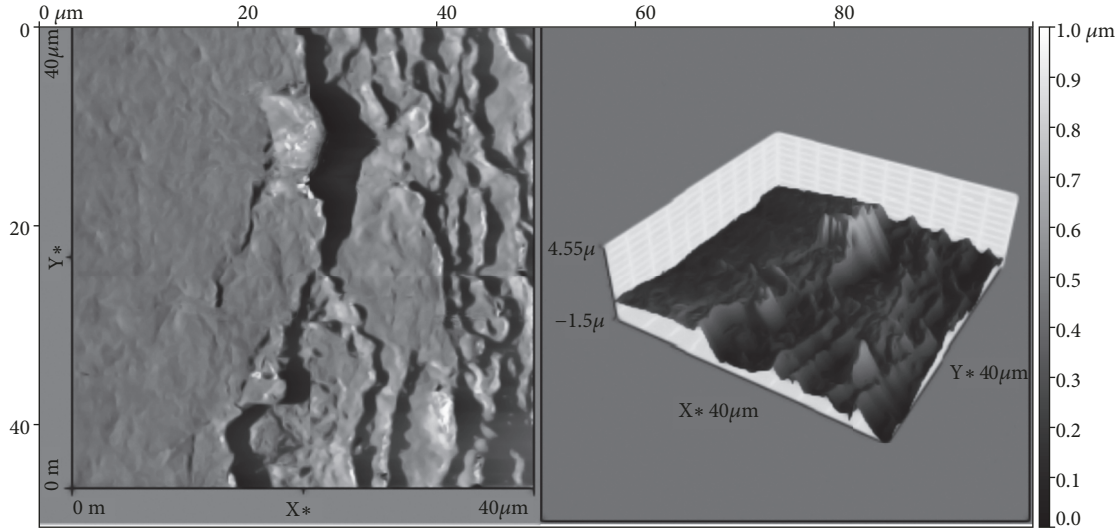


FIGURE 12: This image shows the edge of a sample of 5 LightScribe reduction cycle graphene oxide taken using the SHOCON contact probe. The three-dimensional topography and edge positioning of the sample allow for an approximation of the number of layers of stacked graphene. This sample contains 4-5 layers seen in the various height differentials.

TABLE 1: Data for the LightScribe graphene capacitor.

Resistance (kΩ)	Voltage Stored (V)	RC Time Constant ( $\mu$ s)	Capacitance (pF)
22	9.75	1.00	45.54
66	9.40	1.60	24.24
100	8.55	2.05	20.50
200	6.40	3.95	19.75
300	4.73	4.30	14.33
400	3.72	4.60	11.50
470	3.22	4.20	8.94
500	3.08	4.70	9.40
600	2.68	5.02	8.33
700	2.16	5.10	7.14

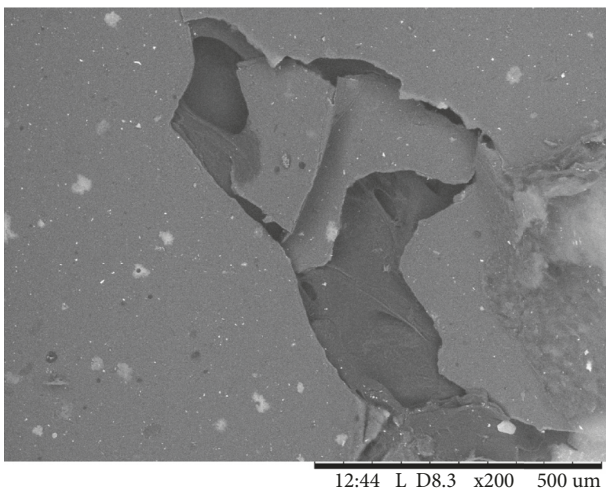


FIGURE 13: SEM image of graphene with stratified layers from 5 LightScribe reduction cycle sample.

measured. The surface charge density and RC time constants were calculated, respectively, with the equations

$$\sigma = \frac{Vk\epsilon_0}{d} \quad (6)$$

and

$$\tau = RC \quad (7)$$

where  $V$  is the average maintained voltage,  $k$  is the dielectric constant of Mylar,  $\epsilon_0$  is the permittivity of free space,  $d$  is the thickness of the Mylar separator, and  $\sigma$  is the surface charge density. A picture of one of the output waveforms can be seen in Figure 15 and the results are summarized in Tables 1 and 2.

The LSGC maintained a voltage of 24.5 times more than that of the CVDGC and had a surface charge density of 25.3 times more than that of the CVDGC. However the CVDGC had an RC time constant that was 29.12 times faster than the LSGC, and an average capacitance of 2.5 times more than the

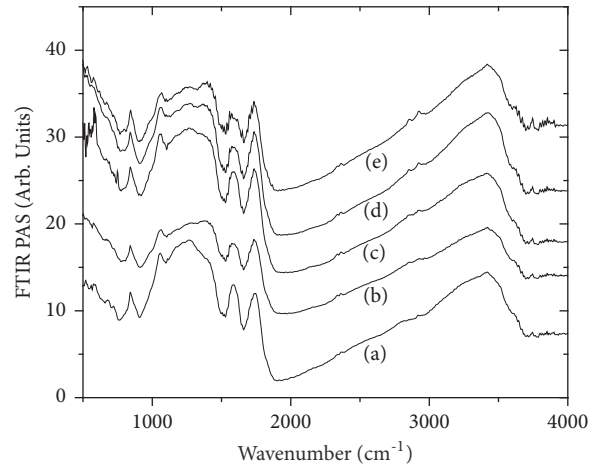


FIGURE 14: FTIR spectrum of homemade graphene oxide after one, two, and five oxygen reduction cycle.

TABLE 2: Data for the commercially purchased CVD graphene capacitor.

Resistance (k $\Omega$ )	Voltage Stored (V)	RC Time Constant ( $\mu$ s)	Capacitance (pF)
22	9.75	1.00	45.54
66	9.40	1.60	24.24
100	8.55	2.05	20.50
200	6.40	3.95	19.75
300	4.73	4.30	14.33
400	3.72	4.60	11.50
470	3.22	4.20	8.94
500	3.08	4.70	9.40
600	2.68	5.02	8.33
700	2.16	5.10	7.14



FIGURE 15: Output waveform of the LSGC connected in series with a 100 k $\Omega$  resistor with an input 10V peak to peak square wave.

LSGC. These results may perhaps show a correlation between the graphene sample thickness and the electron mobility. For instance the LSGC graphene was almost 1000 times thicker than the CVDGC graphene, therefore having more surface

area and maintained a much higher voltage. On the other hand, the thinner CVDGC graphene was allowed to charge and discharge faster, showing higher electron mobility. From these findings we may be able to postulate that perhaps there is a correlation to the thickness of a graphene sample, and its ability to maintain and store more voltage at the cost of electron mobility.

**4.5. Spectroscopic Analysis.** Nanoindentation was performed on the various graphene oxide samples in order to calculate stiffness, hardness, reduced Young's modulus, and the max load applied. This process was done after two and three-dimensional imaging was performed to visualize the topography of the samples after each reduction cycle. A 15 $\mu$ m by 15 $\mu$ m grid of indentations were performed in three separate locations on each sample. Each grid was comprised of 10 indentations yielding a total of 30 spectroscopic points. Table 3 shows the average stiffness, hardness,  $P_{max}$ , and reduced Young's modulus of each sample across the 30 indentations. Therefore, all data discussed hereafter in this section reflects the average values of the data points.

The first samples tested were the unreduced graphene oxide. Although the oven-dried graphene oxide had slightly higher values in every category, the measurements were close

TABLE 3: The statistical analysis results for spectroscopic investigation of various samples. The values displayed are the averages of the thirty data points taken for each sample.

Sample	Stiffness (N/m)	Hardness (GPa)	$E_r$ (GPa)	$P_{max}$ ( $\mu$ N)
0 Reduction Cycle	16.00	3.09	0.81	12.00
1 Reduction Cycle	16.48	3.70	1.18	9.77
2 Reduction Cycles	24.31	4.80	1.50	7.35
3 Reduction Cycles	23.64	5.02	1.61	11.50
4 Reduction Cycles	20.81	5.38	1.62	11.10
5 Reduction Cycles	22.39	5.52	1.61	10.40
Commercial Graphene Oxide	22.80	5.83	1.84	14.10

enough to determine that oven-drying the sample versus air-drying the sample did not significantly affect its material properties or the nanoindentation process.

The first reduction cycle, as expected, led to an increase in the stiffness, hardness, and reduced Young's modulus. The stiffness increased by 2.96% the hardness increased by 17.97%, and the reduced Young's modulus increased by 37.19%, compared to the unreduced graphene oxide.

The second LightScribe reduction cycle generated additional increases in values from a previous reduction cycle, the stiffness increased to 24.31 N/m, a 38.39% increase from the first reduction cycle. The hardness, now 4.80 GPa, showed a 25.88% increase from the previous reduction cycle and a 43.35% increase from the unreduced vacuum-dried graphene oxide sample. Lastly, 23.88% and 59.74% increases in the reduced Young's moduli were seen from the first reduction cycle and the unreduced vacuum-dried samples, respectively, bringing the value of the reduced Young's modulus to 1.50 GPa.

The third reduction cycle showed the first signs that the LightScribe DVD burner was reaching its maximum reduction capabilities. The stiffness decreases by 2.79%, while the hardness and the reduced Young's modulus only increased 4.48% and 7.07%, respectively, from the second reduction cycle. The overall percent increases from the unreduced graphene oxide after the third reduction cycle were 38.55% for the stiffness, 47.6% for the hardness, and 66.12% for Young's modulus.

The fourth and fifth LightScribe reduction cycles signify the maximum reduction capabilities of the DVD burner being reached, with minimal improvement from the third to fourth cycles and almost identical measurements from the fourth to the fifth cycles. The percent increases for the stiffness, hardness, and reduced Young's modulus from the third to the fourth reduction cycles were 12.73%, 6.92%, and 0.62%, respectively. Overall, the increases from the unreduced graphene oxide sample after the fourth reduction cycle were 26.13% for the stiffness, 54.07% for the hardness, and 66.7% for the reduced Young's modulus.

After the fifth and final LightScribe reduction cycle, the stiffness rose to a final value of 22.39 N/m, a 7.31% increase from the fourth cycle. The hardness topped out at 5.52 GPa, only a 2.57% increase from the previous cycle. Lastly, the reduced Young's modulus slightly decreased by 0.62% to a final value of 1.61 GPa. At this point in experimentation, the

maximum effectiveness of the LightScribe DVD burner had been reached, and further reduction cycles would not have altered the material properties a significant amount.

The LightScribe DVD burner was ultimately able to increase the stiffness, hardness, and reduced Young's modulus of the graphene oxide samples. The total percent increases from the unreduced graphene oxide sample to the fifth reduction cycle sample were 33.29% for the stiffness, 56.45% for the hardness, and 66.12% for the reduced Young's modulus.

After testing the final homemade sample, the commercially purchased graphene sample was then spectroscopically investigated via nanoindentation. As expected, the stiffness, hardness, and reduced Young's modulus were all greater than the highest values of the homemade samples (the 5 reduction cycle sample). The stiffness was 22.80 N/m, 1.81% greater than the stiffness of the 5 reduction cycle sample. The hardness was 5.83 GPa, 5.46% greater than the 5.52 GPa hardness of the 5 reduction cycle sample. Lastly, the reduced Young's modulus of the commercial graphene was 1.84 GPa, 13.33% greater than the 5 reduction cycle sample. Although the increase in stiffness, hardness, and the reduced Young's modulus were significant, the measurements were on the same order of magnitude as the 5 reduction cycle homemade graphene sample. This shows the potential for homemade graphene synthesis via DVD burner for reducing the amount of oxygen in graphene oxide.

**4.6. Statistical Analysis.** Examining Figures 16–18 allows for insight into the trends and range of the data, as well as some statistical analysis. First, discussing the stiffness, Figure 16 shows the black standard deviation bars. All of the samples have sections where the error bars, and thus the values overlap. This means that the stiffness between the unreduced sample and the 1 reduction cycle sample, for example, were within one standard deviation of each other. The same holds true for the difference in stiffness between the 1 reduction cycle sample and the 2 reduction cycle sample, the 2 reduction cycle and the 3 reduction cycle sample, etc. However, the second and third reduction cycle samples showed slight increase from the rest. This could be attributed to sample thickness that these two samples could be thicker than the rest. Nonetheless, after the second reduction cycle, we can again say with higher certainty that the graphene oxide sample increased in stiffness from the unreduced sample.

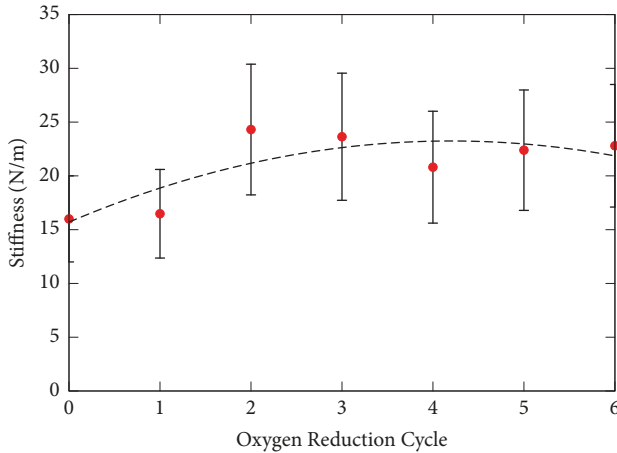


FIGURE 16: This plot compares the stiffness of the sample based on the number of LightScribe reduction cycles. The red points are the average values for the thirty data points taken after each cycle. In order to depict the changing nature of the stiffness, these points were fit using a polynomial function shown above. The error bars depict the standard deviation of the stiffness for the thirty data points taken after each reduction cycle.

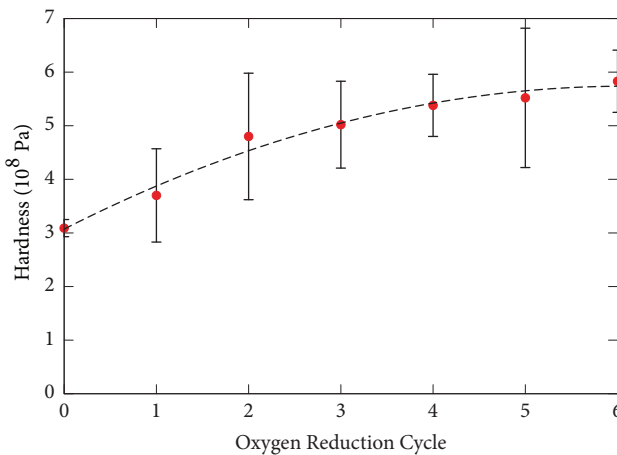


FIGURE 17: This plot compares the hardness of the sample based on the number of LightScribe reduction cycles. The red points are the average values for the thirty data points taken after each cycle. In order to depict the changing nature of the hardness, these points were fit using a polynomial function shown above. The hardness increased for the three reduction cycles before leveling off during the fourth and fifth cycles. The error bars depict the standard deviation of the hardness for the thirty data points taken after each reduction cycle.

The average values and the standard deviations of the hardness shown in Figure 17 must also be investigated. Unlike the stiffness, the standard deviation values of the hardness show greater overlapping regions. It was not until the fourth reduction cycle sample that we can be certain the hardness value increased as it differed from the unreduced sample by more than one standard deviation.

Lastly, Young's modulus data, Figure 18, more clearly exhibited that its value increased during the first and second

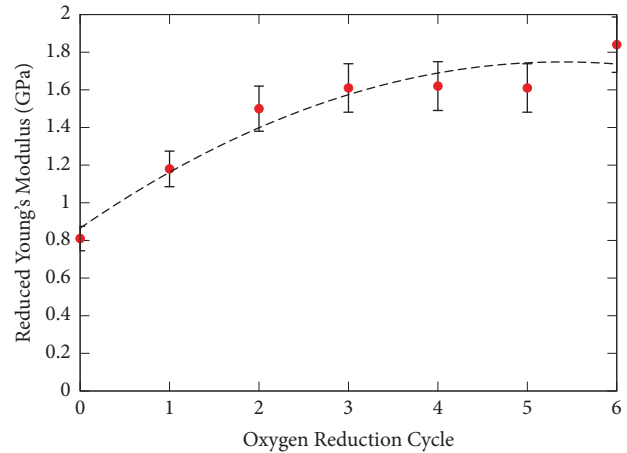


FIGURE 18: This plot compares the reduced Young's modulus of the sample based on the number of LightScribe reduction cycles. The red points are the average values for the thirty data points taken after each cycle. In order to depict the changing nature of the elastic modulus, these points were fit using a polynomial function shown above. The reduced Young's modulus increased for the first three reduction cycles before leveling off during the fourth and fifth cycles. The error bars depict the standard deviation of the reduced Young's modulus for the thirty data points taken after each reduction cycle.

cycles but leveled off after the third cycle. The reduced Young's modulus between the unreduced sample and the 2,3,4 and 5 reduction cycle samples were less than one standard deviation apart. Thus, the increase in the reduced Young's modulus was statistically significant after the first reduction cycle and required one more cycle until the increase in the elastic modulus was certain. Further, similar to the stiffness, the next statistically significant jump in the reduced Young's modulus occurred after the third, fourth, and fifth LightScribe reduction cycles. Thus, after the third reduction cycle, we can again say with higher statistical certainty that the graphene oxide sample's reduced Young's modulus increased from the first reduction cycle. Note that, the values of stiffness, hardness, and reduced Young's modulus for the homemade samples approached that of the commercially purchased sample (shown as the 6th Oxygen Reduction Cycle in Figures 16–18) but none of these values was greater than that of the commercial sample.

## 5. Conclusion

Although significant increases in the stiffness, hardness, and reduced Young's modulus were made via LightScribe reduction, the values obtained in this experiment differ drastically from those of pristine single layer graphene. The values of stiffness and hardness of graphene are not easily standardizable as they depend on the sample's thickness. Young's modulus of pristine graphene, however, is generally accepted to be around 1 TPa [20]. Our sample was definitely not pristine, thus accounting for the dramatically lower reduced Young's modulus. Our results, however, were

still much lower than other nonpristine samples. Work done by Gmez-Navarro [21] revealed Young's modulus of chemically derived single graphene sheets to be approximately 0.25 TPa. Here, the discrepancy in results can be attributed to the fact that our samples generally consisted of 3-5 layer graphene sheets. Also, it is possible that the LightScribe reduction process was not able to convert all of the layers to graphene, thus further lowering the elastic modulus. Importantly, one should note that although our homemade sample differed from the expected Young's modulus of single layer nonpristine graphene by a factor of 100, the commercially purchased sample also differed by the same factor of 100. This speaks to the current and prevalent issue of producing high quality graphene on a large scale. Production of single layer, defect free, pristine graphene proves incredibly challenging, even on a small scale. Improvements in large scale graphene production could usher in a new era of exciting technological and scientific advancements.

In future experiments, these results could be refined and improved. There were numerous sources of error throughout experimentation, one of the largest dealt with the determination of the contact area of the probe. An approximate contact area was determined using manufacturer specifications and force-distance curves, yet the probe tips were all slightly different and the error range in the specifications could vastly affect calculations. Further, the need to use a different sample for each reduction cycle added extra inconsistency to the nanoindentation. The nature of vacuum-drying the samples led to uneven thicknesses, thus every sample was different and comparisons of the mechanical properties across samples became more challenging and less precise. In the future, repeating these tests with different diamond tipped probes could also be beneficial. The DD-ACTA probes used were noncontact mode when imaging, thus using diamond tipped contact probes would be a good way to confirm the results of this project.

Lastly, various conditions in the lab affected the results. Noise arising from light sources, vibrations caused by air conditioning, and a not perfect mechanical vibrations isolation system all reduced the accuracy of the measurements. These factors also affected the images taken, which can be seen via the lines and blurred sections that appear in some images. This problem could be addressed in future experimentation by enclosing the AFM in a vibrationally isolated chamber to reduce these interference factors.

The findings of this research show that DVD burner reduction does show promise in converting graphene oxide to graphene. Using this technique, we have built, as a proof-of-concept, a graphene capacitor exhibiting the great potential of graphene as a supercapacitor for renewable wind and solar energy storages as well as electric cars. The values of stiffness, hardness, and reduced Young's modulus of homemade graphene were on the same order of magnitude as the commercially purchased samples. However, this method is not ideal for attempting to create pristine graphene, which still proves incredibly challenging and will continually be investigated for years to come.

## Data Availability

The data used to support the findings of this study are available from the corresponding author upon request.

## Conflicts of Interest

The authors declare that they have no conflicts of interest.

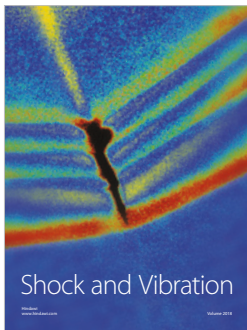
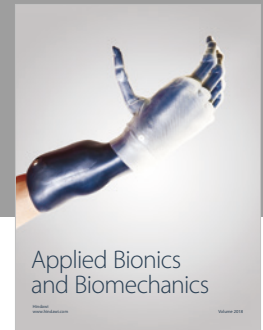
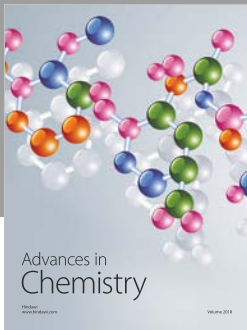
## Acknowledgments

This work was partially supported by the Department of Physics and Astronomy and the School of Sciences and Mathematics at the College of Charleston. The work was also supported by NSF/EPSCoR: SC EPSCoR/IDeA, Award no. 01A-1655740.

## References

- [1] "A Short History of AFM," <http://hansmalab.physics.ucsb.edu/afmhistory.html#history>.
- [2] D. A. C. Brownson, D. K. Kampouris, and C. E. Banks, "An overview of graphene in energy production and storage applications," *Journal of Power Sources*, vol. 196, no. 11, pp. 4873–4885, 2011.
- [3] A. K. Geim and A. H. MacDonald, "Graphene: Exploring carbon flatland," *Physics Today*, vol. 60, no. 8, pp. 35–41, 2007.
- [4] V. C. Tung, M. J. Allen, Y. Yang, and R. B. Kaner, "High-throughput solution processing of large-scale graphene," *Nature Nanotechnology*, vol. 4, no. 1, pp. 25–29, 2009.
- [5] S. Bae, H. Kim, Y. Lee et al., "Roll-to-roll production of 30-inch graphene films for transparent electrodes," *Nature Nanotechnology*, vol. 5, no. 8, pp. 574–578, 2010.
- [6] K. S. Kim, Y. Zhao, and H. Jang, "Large-scale pattern growth of graphene films for stretchable transparent electrodes," *Nature*, vol. 457, no. 7230, pp. 706–710, 2009.
- [7] "Slim External Aluminum Slot-Loading BDXL Blu-Ray Writer," <http://www.pawtec.com/lightscribe/>.
- [8] JPK Instruments, "A Practical Guide to AFM Force Spectroscopy," 2008.
- [9] "Graphene Coated Aluminum," <https://graphene-supermarket.com/Graphene-on-Aluminum-Foil.html>.
- [10] Atomic Force Microscope, <http://www.nanosurf.com/?content=040230>.
- [11] P. Hermanowicz, M. Sarna, K. Burda, and H. Gabrys, "AtomicJ: An open source software for analysis of force curves," *Review of Scientific Instruments*, vol. 85, no. 6, Article ID 063703, 2014.
- [12] X. Li, H. Gao, C. J. Murphy, and K. K. Caswell, "Nanoindentation of Silver Nanowires," *Nano Letters*, vol. 3, no. 11, pp. 1495–1498, 2003.
- [13] W. D. Nix, *Materials Science and Engineering: A Structural Materials: Properties, Microstructure and Processing*, Stanford University, Department of Materials Science and Engineering, Stanjbrd CA, USA, 1997.
- [14] "Graphene Oxide Solution," [https://graphene-supermarket.com/Highly\\_Concentrated\\_Graphene\\_Oxide\\_60-ml.html](https://graphene-supermarket.com/Highly_Concentrated_Graphene_Oxide_60-ml.html).
- [15] M. F. El-Kady and R. B. Kaner, "Scalable fabrication of high-power graphene micro-supercapacitors for flexible and on-chip energy storage," *Nature Communications*, vol. 4, article 1475, 2013.

- [16] “AppNano ACLA Probe,” <http://www.appnano.com/>.
- [17] “AppNano SHOCON Probe,” <http://www.appnano.com/>.
- [18] AppNano DD-ACTA Probe, <http://www.appnano.com/download/DD-ACTA.pdf>.
- [19] K. Krishnamoorthy, M. Veerapandian, K. Yun, and S.-J. Kim, “The chemical and structural analysis of graphene oxide with different degrees of oxidation,” *Carbon*, vol. 53, pp. 38–49, 2013.
- [20] K. S. Novoselov, V. I. Fal’ko, L. Colombo, P. R. Gellert, M. G. Schwab, and K. Kim, “A roadmap for graphene,” *Nature*, vol. 490, no. 7419, pp. 192–200, 2012.
- [21] C. Gómez-Navarro, M. Burghard, and K. Kern, “Elastic properties of chemically derived single graphene sheets,” *Nano Letters*, vol. 8, no. 7, pp. 2045–2049, 2008.



Hindawi

Submit your manuscripts at  
[www.hindawi.com](http://www.hindawi.com)

